Two-step sintering of alumina nano-powders: A discrete element study

Brayan Paredes-Goyes, Aatreya Manjulagiri Venkatesh, David Jauffrès, Christophe L. Martin

Two-step sintering of alumina nano-powders: A discrete element study

Brayan Paredes-Goyes[a], Aatreya Manjulagiri Venkatesh[a], David Jauffres[a], Christophe L. Martin[a]

[a]*Univ. Grenoble Alpes, CNRS, Grenoble INP, SIMaP, F-38000 Grenoble, France*

Abstract

Avoiding grain growth during sintering of ceramic nano-powders is of great technological interest. Although two-step sintering is an effective technique to achieve this goal, the mechanisms at play are not well understood. This study adapts our previous discrete model to investigate the conventional and twostep sintering of nano-powders. The densification and grain growth results agree qualitatively well with experimental data on α-alumina. Simulations confirm that faster heating rates retard grain growth in conventional sintering of nano-alumina. Our results support the hypothesis that the success of nano-alumina two-step sintering relies on the sharp increase in the activation energy of the grain boundary mobility at low temperatures. Simulations indicate a transition temperature of 1100° C and that at least a 2.5-fold increase in activation energy is required to explain the suppression of grain growth. The relative weights of surface diffusion and of grain boundary motion for grain growth are clarified.

Keywords: nano-powders, two-step sintering, grain growth, alumina, discrete element method

1. Introduction

Solid-state sintering produces dense or density-controlled materials from ceramic or metallic powders using thermal energy. The driving force for sintering is the reduction in the total interfacial energy of the system [1, 2]. There are two contributions to the reduction of the product γA, where γ is the average interface energy and A is the total interface area of the system: $A\mathrm{d}\gamma$ and $\gamma\mathrm{d}A$. Thus, during sintering, a coupling between two mechanisms occurs: densification that reduces interfacial energy ($\mathrm{d}\gamma$) by replacing solid-gaz interfaces by less energetic solid-solid interfaces, and coarsening that reduces interfacial area ($\mathrm{d}A$) [1, 3]. In general, materials scientists and practitioners favor densification while attempting to limit coarsening.

This is especially true when starting from nano-powders (typically < 100 nm grain size) that have great scientific and technological interest. The short diffusion distances in nano-powders inherently favor both grain growth and densification kinetics. Yang et al. [4] have recently demonstrated that the densification of nano-sized α-alumina powders proceeds through the same dominant mechanism as that involved in the sintering of micron-sized alumina, namely grain boundary diffusion. For nano-powders, keeping submicronic size grains while ensuring a nearly dense material is challenging. A fast heating rate is an efficient processing method to enhance densification over grain-growth. It is based on the usual condition for most materials that activation energies of grain boundary diffusion along the boundary (densification) are higher than that

of grain boundary diffusion perpendicular to the boundary (grain growth) [2]. Fast heating rates may be effectively combined with a modification of the thermal cycle, using a combination of high and low temperatures. This so-called two-step sintering technique may be declined in several variants [5]. Following the two-step approach proposed by Chen and Wang on Y2O3 [6], Yang et al. [4, 7] have recently demonstrated the effectiveness of two-step sintering technique to densify Al2O3 ceramic 30 nano-powders while keeping small grain size (≈ 40 nm).

The reason for the suppression of grain growth in the two-step sintering of α-alumina is still under study. For Y_2O_3 Chen and Wang have argued that it is possible, at low temperature, to almost eliminate grain boundary motion while keeping grain boundary diffusion active. Their argument is based on the theory proposed by Gottstein et al. that triple junctions can drag grain boundary motion at low temperature [8]. In particular, these authors have been able to confirm experimentally their theoretical predictions by measuring triple junctions mobility on Zn and Al tricrystals [8, 9]. Accordingly, a transition in grain boundary mobility between grain boundary controlled motion at high temperature and triple junction controlled motion at low temperature is expected. Such a mobility transition has indeed been observed in Y_2O_3 polycrystals [10] thus confirming the suggested scenario. For α-alumina, the interplay between surface diffusion, grain boundary diffusion along and perpendicular to the grain boundary is not sufficiently documented to unambiguously propose a clear scenario. This task is made more difficult by the fact that, in conjunction with temperature changes, the microstructure itself

undergoes profound alterations. The initial material is granular and begins as an assembly of discrete particles that interact with small contacts. It ends as a set of grains with small isolated pores remaining. Numerical modeling can provide a better understanding of the grain growth of nano-powders during conventional and two-step sintering. At the atomistic scale using molecular dynamics, Ding et al. [11] provided insights into the mechanisms of neck and grain growth during the sintering of 2 and 3 nanoparticles. Depending on the crystalline orientation of the grains, they observed the disappearance of the grain boundary and the switch of neck growth mechanisms halfway during the sintering process. At the particle scale, Benabou and Wang [12] used the surface evolver approach to simulate the sintering of up to 40 particles. The detailed description of the surfaces allowed them to observe the elimination of pores and the disappearance of small particles by grain growth. Monte Carlo methods can also model efficiently the sintering of a reasonable number of initial particles with realistic interactions [13]. There is a drastic decrease in particle number with coarsening. Thus, a representative packing with a large initial number of particles is needed to properly study the microstructure evolution in simulations. Using discrete element modeling (DEM), we have already successfully investigated grain growth occurring during the sintering of large packings of micronic α-alumina particles (up to 400 000) [14].

The aim of this study is to extend our previous work to analyze grain growth and densification of nano-sized α-alumina during conventional and two-step sintering. Section 2 summarizes our model with some modifications to correctly model nano-powders. The simulations and comparison with experimental data

of conventional sintering are presented in Section 3. These simulations are performed for different heating rates. The evolution of density, densification rate and grain size with temperature are reported and critically compared to experimental data from Yang et al.[4]. The volumes transferred by surface diffusion and grain boundary migration are quantified. Section 4 presents two-step sintering simulations, their comparison to experimental data and a discussion on the origin of the absence of grain growth.

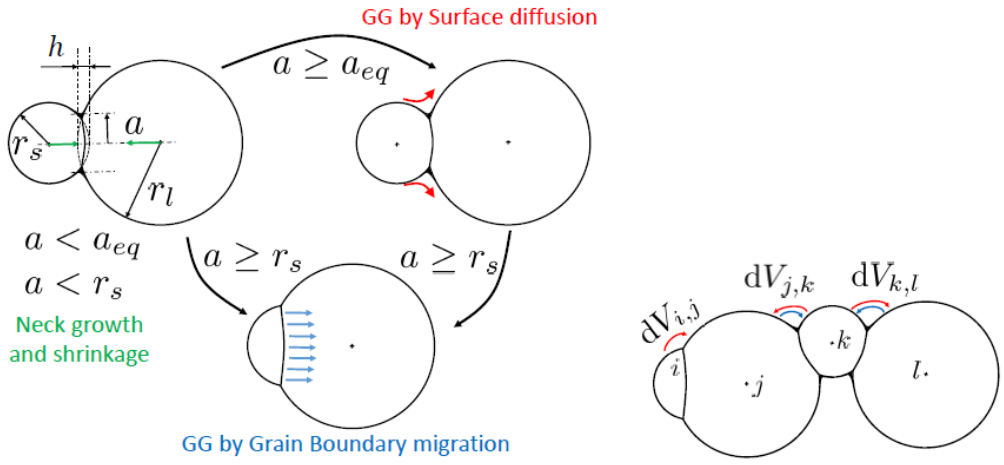

Figure 1: Graphical summary of the model. (a) Grain growth (GG) by Surface diffusion is activated after neck growth reaches the equilibrium configuration. Grain growth by Grain Boundary migration can be attained after GG by surface diffusion or directly after neck growth. (b) Volume exchange dV is always from small to large particle when the small particle has only one contact (i,j). For small particles with more than one contact ((j,k) and (k,l)), a large particle may give volume dV to a small one with probability $P_{s,l}$.

2. Model description

The details of the model (contact laws, contact size, grain growth model) can be found in [14]. Here we summarize its main ingredients and report the material

parameters used in the simulations. In DEM, particles are represented as spheres that are progressively truncated at contacts with other particles as sintering proceeds. The powder compact is modeled as a 3D random assembly of spherical particles interacting through their contacts. At each time step, all contacts are considered and contact forces are calculated and summed up for all particles. Particle velocities and new positions are updated using a velocity-Verlet algorithm. As proposed in our earlier work [15] and classically adopted by other researchers in DEM simulations of sintering [16, 17, 18, 19, 20, 21], normal contact forces appear between particles including two components. The viscous component introduces the diffusion coefficient along the grain boundary $D_{GB} = D_{0GB} \exp \frac{-RTQ_{GB}}{}$ with temperature dependence (activation energy Q_{GB}). This component opposes the relative motion between the two particles. The tensile component (also known as the sintering force) introduces the surface energy γ_S. The expression of the normal force is derived from results obtained by Bouvard et al. [22] and Pan et al. [23] and accounts for sintering by coupled grain boundary diffusion and surface diffusion, typical of solid state sintering of oxide ceramics. The contact radius a is calculated here from the model of Pan et al. [23] for particles of different sizes. The size of the contact plays an important role in the model as it dictates the transition from one mechanism to another. The equilibrium contact radius a_{eq}, at which the sum of the grain boundary and surface energies reaches a local minimum, is given by the equilibrium dihedral angle Ψ_{eq}. When the contact size becomes larger than a_{eq}, grain growth (GG) by surface diffusion becomes active, unless the smallest particle is itself smaller than the contact, in which case GG by grain boundary migration becomes active (Fig. 1a).

Grain growth is modelled by simply considering that an exchange of matter dV results in a radius decrease and a radius increase for the two particles in contact. The flux of matter $\frac{\mathrm{d}V}{dt}$ originates from two contributions: *Surface* (*S*) diffusion or *Grain Boundary Migration* (*GBM*). The surface diffusion contribution writes:

$$\left(\frac{\mathrm{d}V}{\mathrm{d}t}\right)_S = -4\pi\frac{\delta_S D_{0S}\exp\frac{-Q_S}{RT}}{k_B T}\gamma_S\Omega\frac{\frac{1}{r_l}-\frac{1}{r_s}}{r_l+r_s-h}a \qquad a \geq a_{eq} \tag{1}$$

where h is the geometric indentation between the two spherical discrete elements (Fig. 1a), k_bT has the usual meaning, Ω is the atomic volume and δ_S is the thickness of the diffusion layer. The Grain Boundary Migration diffusion contribution writes:

$$\left(\frac{\mathrm{d}V}{\mathrm{d}t}\right)_{GBM} = -2M_{0GB}\exp\frac{-Q_{GBM}}{RT}\gamma_{GB}\left(\frac{1}{r_l}-\frac{1}{r_s}\right)\left[\pi a^{*2}\right] \qquad a \geq r_s \tag{2}$$

with a^* the contact radius when Grain Boundary Migration becomes active. Both Eqs. (1) and (2) have temperature dependence through Arrhenius law with pre-exponential factors D_{0S} and M_{0GB}, and activation energies Q_S and Q_{GBM}, respectively. Note that as sketched in Fig. 1a, the two contributions are mutually exclusive, i.e. only one (or none) is active at a given point for a contact.

When Grain Boundary Mobility is active ($a > r_s$), by default the volume of matter flows from the small to the large particle. We have observed that this simplistic assumption triggers abnormal grain growth in our simulations for nano-sized particles. As compared to our previous work in [14], we have thus added an ingredient to the model that controls the occurrence of abnormal grain growth by introducing some departure from this default condition. This is carried out by stating that a small particle that has two or more contacts (particle k in Fig. 1b) has a probability $P_{s,l}$ to have positive matter flux from the larger one. This scenario is supported by finite difference simulations on particles of different

sizes for two or three particles in contact [24]. For nanosized particles, these authors reported the intriguing result that a small particle in contact with two larger ones can develop some resistance to invasion. In particular, they showed that, rather than shrinking, the small particle grows at the expense of the two larger ones. Eventually, the small particle always disappears as the boundary migrates. This result was further refined by molecular dynamics simulations of nanoparticles sintering [11] that showed that many different scenarios could exist, depending mainly on the initial crystalline misalignment between particles. These results indicate that local curvature (or grain size for spherical grains) may not always dictate the grain boundary velocity when departing from the simplistic model of two grains. This is consistent with recent experimental results that reveal that there is no observed relationship between grain boundary velocity and curvature in polycrystalline Ni with multiple grain boundaries [25]. These scenarios cannot be realistically included in DEM simulations with several hundreds of thousands of particles. The probability $P_{s,l}$ that a small particle (with more than one contact) can temporarily eat away a larger one accounts for these alternative scenarios in a very simple manner. We set this value in all simulations to $P_{s,l} = 1/4$, and observed that this was sufficient to prevent abnormal grain growth.

3. Sintering at constant heating rate

The model described above was applied to simulate the sintering of αAl_2O_3 nanopowders, which has been thoroughly examined experimentally in [4, 7]. Starting from a powder cold-compacted to a green density of 0.48, sintering was carried out at various heating rates. The initial powder (before compaction) was

observed by TEM at approximately 5 nm in size, with a narrow initial grain-size distribution (standard deviation normalized by the average grain size = 0.23). Numerical specimens were prepared to reproduce this initial green packing. We observed in our simulations that applying a 500 MPa axial stress on this packing already triggered at room temperature some grain coarsening (i.e. $a \geq a_{eq}$ or $a \geq r_s$) due to surface energy effects. This is because adhesive forces induce local elastic strains that are far from negligible for nano-powders. Using the DMT model, which is well adapted for hard and small particles [26, 27], the equilibrium contact radius a of two identical spheres of radius r with Young's modulus E and Poisson's ratio ν writes:

$$\frac{a}{r} = \frac{3}{2}\pi\frac{\gamma_s}{r}\frac{1-\nu^2}{E} \qquad (3)$$

yielding a value $a/r \approx 0.17$. Eq. (3) is derived for two particles without external stress. Adding external stress further increases strain at contacts, which should lead to irreversible grain deformation and coalescence even below 800° C. Thus, we started our sintering simulations with an average grain size of 10 nm, which is in good accordance with SEM observations [4]. Packings made of 400 000 randomly located particles, with an initial relative standard deviation of the grain-size distribution of 0.23 were compacted up to 0.50 relative density in a periodic simulation box to obtain the starting green powder. This large number of initial particles is needed to obtain statistically meaningful results at the end of sintering when a large number of particles have disappeared (see Appendix A).

Material parameters used in the simulations are summarized in Table 1. Activation energies for grain boundary diffusion, Q_{GB}, surface diffusion, Q_S, and grain boundary mobility, Q_{GBM}, were taken directly from the literature, and are

the same as those used for micronic α-alumina powder sintering in [14]. The prefactor of the grain boundary diffusion coefficient was adjusted to fit the experimentally observed relative density at T_1 = 1150° C for a 10 °C/min heating rate. The partially sintered packing obtained at this temperature is used for two-step sintering simulations in section 4. The prefactor of the surface diffusion coefficient was chosen to keep the same ratio of the grain boundary diffusion to surface diffusion (ξ = 0.001) as in our previous work for a temperature of 1350° C. For small values of ξ (associated with the lower temperatures simulated here), the work of Bouvard and McMeeking [28] suggests that the tensile term in the normal force expression depends only weakly on ξ. This ensures that the parameters of the sintering model used for micronic sizes remain valid [14]. Note that the activation energies in Table 1 are consistent with the range proposed in [4] for nano-powders.

Fig. 2 shows the evolution of the densification rate dρ/dt for the three simulated heating rates (3, 5 and 10° C/min). Fig. 2 indicates that, owing to the very small size of the starting powders, densification is already active at 800° C. This may be understood by recognizing that the sintering force expression in our model leads to a time normalization (before coarsening mechanisms start to play a role) that scales with the mean particle size, G to the power 4: $\tau \propto \langle r \rangle^4$. This is in line with classic analytical models that lead to densification rates scaling with G^4 [33].

$\delta_{GB}D_{0GB}$ (m³/s)	1.04x10⁻¹¹	Q_{GB} (kJ/mol)	475 [29]
D_{0S} (m²/s)	7.2x10⁻⁰⁵	Q_S (kJ/mol)	313.8 [30]
M_{0GB} (m³/(N.s))	0.02 [31, 14]	Q_{GBM} (kJ/mol)	443 [31]
Ψ_{eq} (°)	138 [32]	Ω (m³)	2.11x10⁻²⁹ [30]
γ_S (J/m²)	0.905 [30]	γ_{GB} (J/m²)	$2\gamma_S \cos(\Psi_{eq}/2)$

Table 1: Material parameters used for α-alumina.

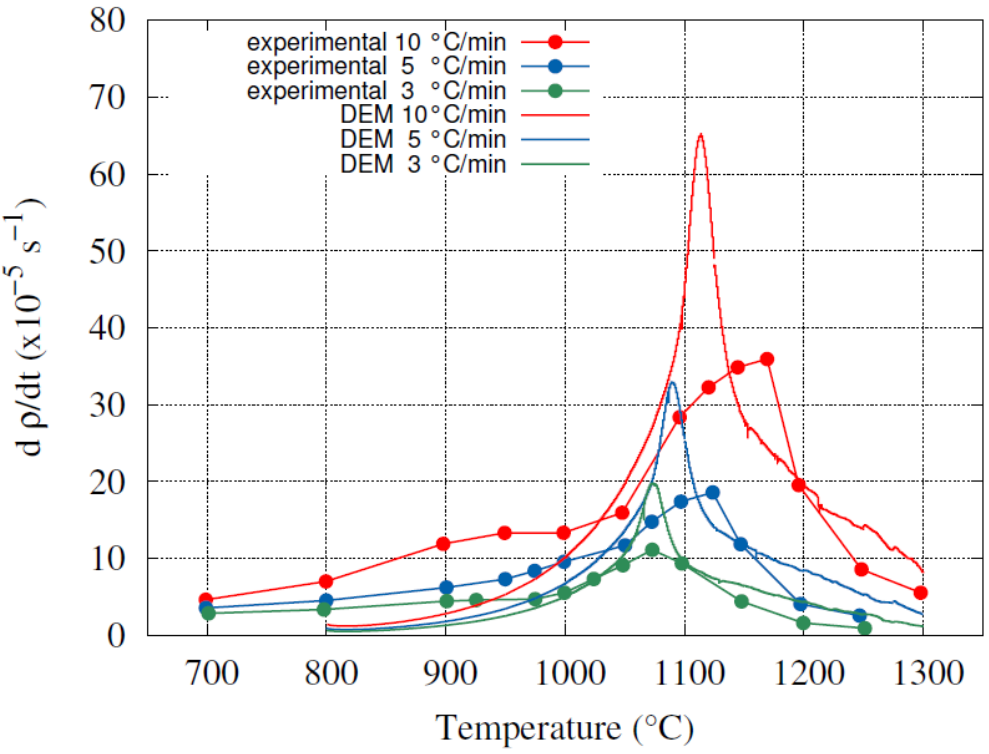

Figure 2: Densification rate evolution with temperature for three heating rates: 3, 5 and 10° C/min. Experimental data for α-alumina is from [4]

.

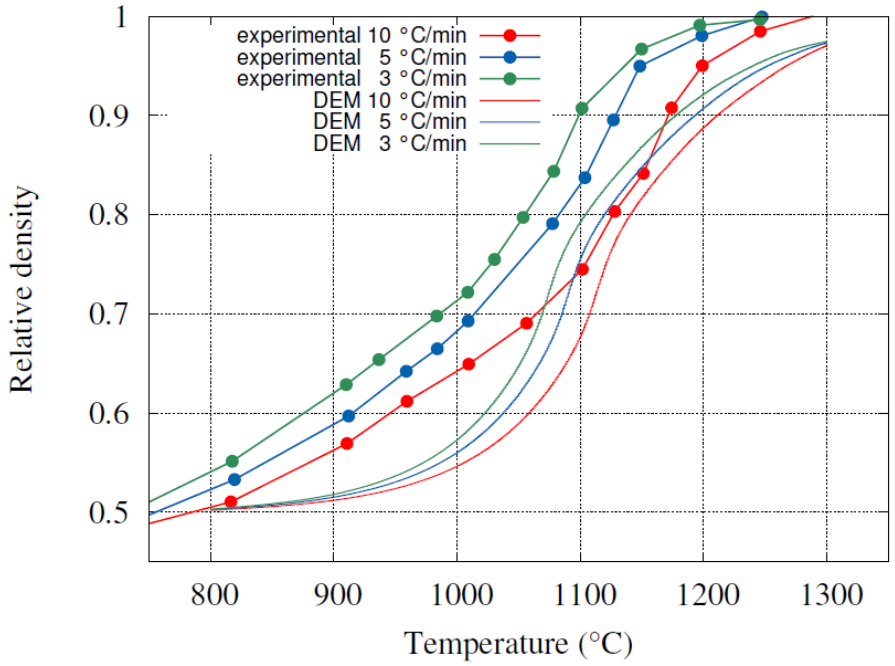

Figure 3: Relative density evolution with temperature for three heating rates: 3, 5 and 10° C/min. Experimental data for α-alumina is from [4]

While our simulations indicated that the heating rate has a minor influence on the sintering of micro-alumina [14], this is no more the case for nano-alumina. For all three heating rates, the densification rate increases to a maximum and decreases to very small values when full density is approached. The temperature at which this maximum occurs increases with increasing heating rates. A higher heating rate is associated to a higher maximum densification rate: the peak densification rate at 10° C/min is three times as fast as that at 3° C/min. This is the result of two effects. First, Fig. 3 shows the evolution of density with temperature. It indicates that at a given temperature, a faster heating rate results in a lower relative density, thus keeping the driving force for densification

higher. Second, Fig. 4 shows that grain growth arises at higher temperatures as the heating rate increases.

The occurrence of the maximum densification rate is well correlated in all three simulations to the initiation of grain growth. Fig. 4 indicates that the heating rate has a clear effect on the final grain size.

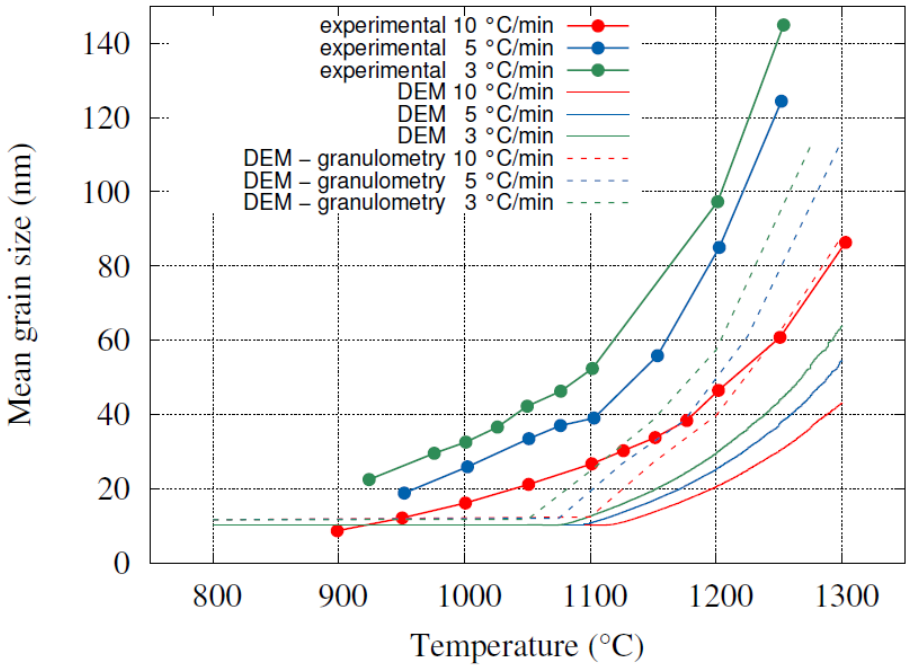

Figure 4: Mean grain size evolution with temperature for three heating rates: 3, 5 and 10° C/min. Experimental data for α-alumina is from [4]. The dashed lines represent the mean grain size of the DEM packings calculated by image analysis (granulometry algorithm).

Figs. 2, 3 and 4 include experimental data from [4] for comparison. Recall that the only material parameter that was adjusted was the prefactor of the grain boundary diffusion coefficient to fit approximately the experimental relative density for 10° C/min at T_1 = 1150° C. The comparison demonstrates that the DEM simulations are able to capture qualitatively well all relevant experimental

features. In particular, the bell shape of the densification rate with temperature (Fig. 2), the S shape of the evolution of the density with temperature (Fig. 3), and the concave shape of the grain growth (Fig. 4). However, some quantitative differences are clear. In particular, the DEM simulations underestimate the initial sintering activity of the powder at low temperature (both densification rate and grain growth). Because of the strong model assumptions, it was not possible to fit the densification curves at both low and high temperatures. In particular, the following model assumptions may not be valid: homogeneous packing (nano powders are prone to agglomeration), presence of defects, impurities or or irregularly shaped particles (due to high-energy ball milling [4]). The choice was made to fit densities at high temperatures and consequently the densification is underestimated at low temperatures. For grain growth, the delayed initiation is linked to our simplistic assumption that surface diffusion and grain boundary motion are mutually exclusive and abruptly starts only when the contact radius is above a critical radius (Fig. 1). This results in DEM relative density curves lagging behind the experimental curves at low temperature. In addition, we observed that the mean grain size of DEM packings calculated using image analysis on 3D images generated from the simulations (dashed lines in Fig. 4) results in larger grain size that are in better accordance with experimental data. This methodology, comparable to the one used by [4], is detailed in Appendix B.

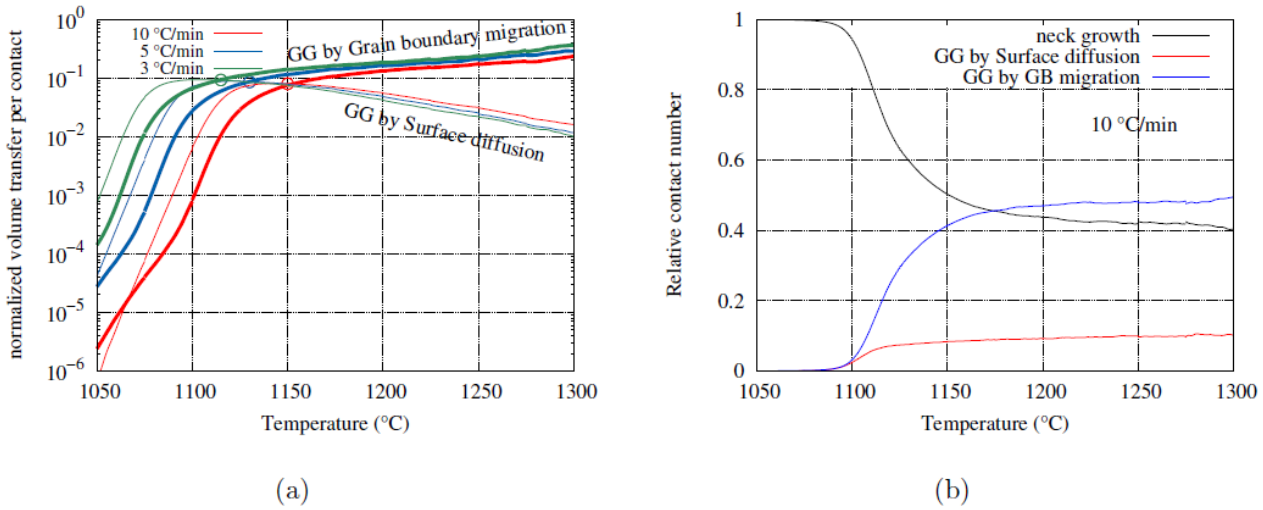

Figure 5: DEM simulation results. a) Evolution of the mean volume transferred per contact (normalized by the mean volume of particles) with temperature for three heating rates: 3, 5 and 10° C/min. Two contributions for grain growth (GG) are shown: surface diffusion (Eq. (1)) and grain boundary migration (Eq. (2)). Circles indicate the temperature at which grain boundary migration contribution exceeds surface diffusion contribution. b) Evolution of the relative contact number (normalized by the total number of contacts) for each possible status: neck growth, GG by surface diffusion and GB migration for 10° C/min.

Keeping in mind these discrepancies with experimental data, the mechanisms that lead to grain growth in nano-powders can still be analysed using the detailed results of DEM simulations. Fig. 5a shows on a log-scale the mean volume transferred per contact at a given temperature. It is separated into the two contributions given by Eqs. (1) and (2). Fig. 5a indicates that at low temperature, surface diffusion is the main contributor to grain growth, although this contribution becomes significant only above 1070-1100° C, depending on the heating rate. This is in line with the general view that at lower sintering temperatures, surface diffusion dominates matter redistribution during grain growth. Grain boundary migration becomes dominant at higher temperature

with large transfer of volumes from one particle to another (compared to the actual volume of particles). Fig. 5b confirms this result. It shows the evolution of contact status as temperature increases for the 10° C/min heating rate (it is representative of all 3 heating rates). At low temperatures, all contacts are in the initial neck growth status and gradually shift to grain growth by surface diffusion and by grain boundary migration. Note that below 1100° C, Fig. 5b shows that very few contacts contribute to grain growth, thus explaining the very small volume transfer indicated by Fig. 5a for these temperatures at 10° C/min.

Because new contacts arise between particles all along sintering due to densification and rearrangement of particles, neck growth and shrinkage are still active leading to the continuation of densification. These results are similar qualitatively to those obtained for micronic powders [14]. It shows that conventional sintering models can be applied to nano-powders and reproduce their very good sinterability and significant grain growth.

Fig. 5a also explains the results shown in Fig. 4 which indicate the beneficial effect of higher heating rates to retard grain-growth. The shift from surface diffusion to grain boundary migration triggers significant grain growth in our model. This shift arises at higher temperature for faster heating rates. We believe that our model underestimates grain growth by surface diffusion at low temperature (as proved by the grain size curves lagging behind the experimental curves at low temperature, Fig. 4). Still, Fig. 5a points to an interesting lever to retard grain-growth: delaying the migration of grain boundaries, which is much more effective than surface diffusion for grain growth.

A practical alternative to retard the migration of grain boundaries is to actually freeze this mechanism by using two-step sintering, which takes advantage of low

temperatures in a second prolonged isothermal stage [5]. This is studied in the next section.

4. Two-step sintering

Numerical samples originating from constant heating rate simulations were retrieved for a second sintering step at a lower constant temperature. In line with the experimental procedure adopted in [4], table 2 lists the main parameters of these simulations. The densities obtained in simulation at the end of the first step (ρ_c) are lower than the experimental densities (Fig. 3). As input for the second step, we opted to use the microstructure obtained at the experimental temperature T_1 instead of the microstructure obtained at the same density of experiments.

First, we ran the simulations of the second step (lower temperature) with the same activation energies as in the first step (higher temperature). In that case, considerable grain growth is observed. However, Gottstein et al. [8] observed that at low temperatures the motion of the grain boundary is controlled by the 3-grains junction lines that have a higher mobility activation energy. This was the principle employed by Chen and Wang [6] to propose for the first time the variant of two-step sintering used in the present study. The effect of the junction mobility results in a higher apparent activation energy of the grain boundary motion below a transition temperature. This has been measured experimentally for aluminum crystals [9], tungsten [34] and yttria-stabilized zirconia [10]. The multiplicative factor of the observed increase in activation energy is between 1.9 and 2.6. Yang et al. [4] suggested that this activation energy increase could also

occur in the case of α-alumina. Thus, we have tested a higher activation energy of grain boundary migration Q_{GBM} for low temperatures in our simulations.

	ρ_c	G (nm)	T_1 (° C)	T_2 (° C)
10° C/min	0.82	13.6	1150	1025
5° C/min	0.76	10.7	1100	975
3° C/min	0.72	10.2	1075	950

Table 2: Main parameters of the second-step sintering. ρ, G : density and mean grain size attained in the first step. T_1: temperature at which this density was obtained, and T_2: temperature of the second isothermal sintering step.

Fig. 6 shows the grain boundary mobility as a function of temperature, where the slope represents the value of the activation energy Q_{GBM}. Data points are collected from the literature [31, 35, 36, 37, 38, 39]. For the first step, we choose Q_{GBM}=443kJ/mol according to α-alumina experimental data at high temperatures (red line). To the best of our knowledge, no activation energies for junction mobility or for grain boundary mobility at temperatures below 1325° C are reported in the literature. Based on the data for other materials commented above, we choose an activation energy 2.5×Q_{GBM} (blue line) for the second step. Regarding the transition temperature, there is also no experimental data for alumina. Based on our simulation results of grain size (Fig. 4), we choose T = 1100° C as below this temperature grain growth is negligible. Simulations indicate that using lower transition temperatures, very high nonphysical values of activation energy (> 3 × Q_{GBM}) would be needed to suppress grain growth. We

corroborated that using the selected activation energy and transition temperature in the second step has negligible effects in the results of the first step.

Simulations of the second step were carried out for the three heating rates studied in the previous section, using 2.5×Q_{GBM} at low temperatures. Fig. 7 illustrates the 3D microstructural evolution from DEM simulations for conventional and two-step sintering for the heating rate 5° C/min. From 0.50 to 0.76 relative density (T = 800° C → T_1 = 1100° C), the number of particles decreases (from 400 000 to 263 000) due to some volume transfer but without significant increase of the mean grain size. Conventional sintering (T_1 = 1100° C → T = 1175° C) leads to grain growth as already indicated in Fig. 4 with a further decrease in particle number (from 263 000 to 36 000). In contrast, two-step sintering (T_2 = 975° C) keeps the same number of particles and mean grain size.

Fig. 8 shows the grain size-density trajectories obtained by simulations for both conventional sintering and in two steps. The simulations of two-step sintering were able to reproduce the experimental results, i.e. annihilating the grain growth while continuing densification. During the second step a slight grain growth is observed at 10° C/min, while no grain growth occurs for the two slower heating rates. This is due to a combined effect of much higher grain boundary mobility for 10° C/min (higher T_2, table 2 and Fig. 6) and a more advanced state of the microstructure on the sintering trajectory at the beginning of the second step in our simulations, which favors grain growth.

In order to inspect the alterations produced by two-step sintering on grain growth, Fig. 9 shows the volume transferred by surface diffusion and grain

boundary motion for one and two-step sintering. In accordance with Fig. 8, the grain growth from both mechanisms is lower in two-step than in conventional sintering. The decrease of the volume transferred by surface diffusion is essentially due to the lower temperature employed in two-step sintering. One way to further decrease it is to use a powder with a narrow initial size distribution as indicated for nanopowders by Fang et al. [40] and verified by simulations in micro-alumina in our previous work [14]. The decrease of volume transmitted by grain boundary migration is much more substantial (Fig. 9) and caused both by the reduction of process temperature and, mainly, by the increase of the associated activation energy (Fig. 6). Therefore, our simulations suggest the validity of the hypothesis proposed by Yang et al. [4] on the grain boundary mobility transition as a cause for the effectiveness of the α-alumina two-step sintering. This applies since the activation energy of the alumina grain boundary diffusion, that governs densification, is assumed constant and is lower than the activation energy of GB mobility. We studied the effect of different values of the activation energy of the GB mobility (Fig. 10). Simulations confirm that an increase of at least $2.5\times Q_{GBM}$ is necessary to suppress grain growth. We also observed that keeping the same value for the activation energy ($1.0 \times Q_{GBM}$, pink curve), the two-step trajectory actually accelerates grain growth as compared to conventional sintering for 10° C/min (dashed red line). This is again due to the fact that the activation energy of the grain boundary mobility is lower than that of the grain boundary diffusion. The sintering temperature being low (T_2 = 1025° C), a significant grain growth is obtained after a long sintering time (170h), which is contradictory to experimental data for two-step sintering. The densification kinetics is very slow in this case, due to the significant growth of

grains. For two-step sintering and 2.5×Q_{GBM}, the times indicated (in hour) in Fig. 10 are in line with experimental data, which report full densification after 40 hours of sintering in the second step [4].

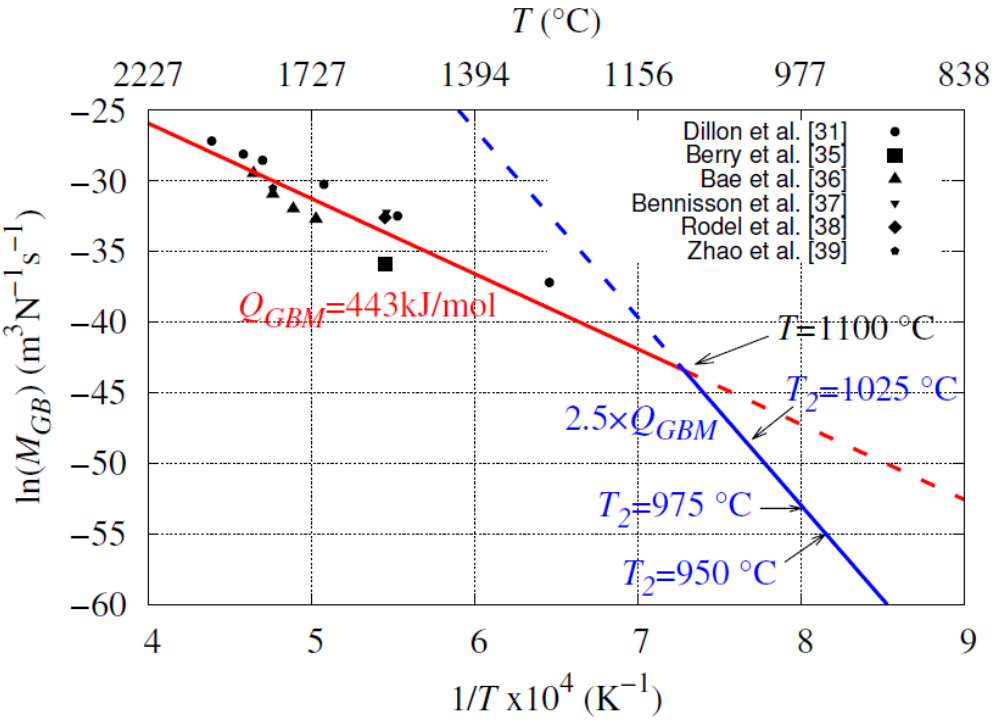

Figure 6: Grain boundary mobility of α-alumina with data points from the literature [31, 35, 36, 37, 38, 39]. Q_{GBM}=443kJ/mol (red line) is the standard value used for the first step. An increase of 2.5 × Q_{GBM} (blue line) is considered for the second step with a transition temperature at T =1100° C. T_2 is the temperature of the second step according to table 2.

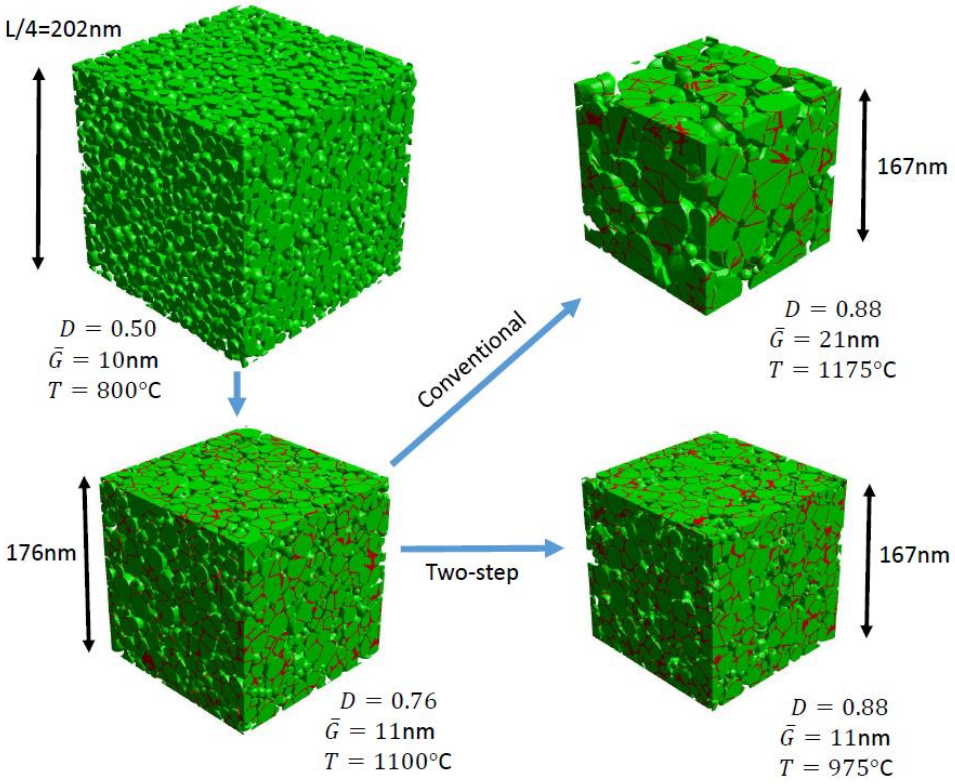

Figure 7: Evolution of DEM microstructures at 5° C/min heating rate . The sintered necks are represented by two inverted tori tangent to each particle [14]. Grain boundaries are shown in red. Only a portion of the total simulation cube (L^3) is shown for clarity.

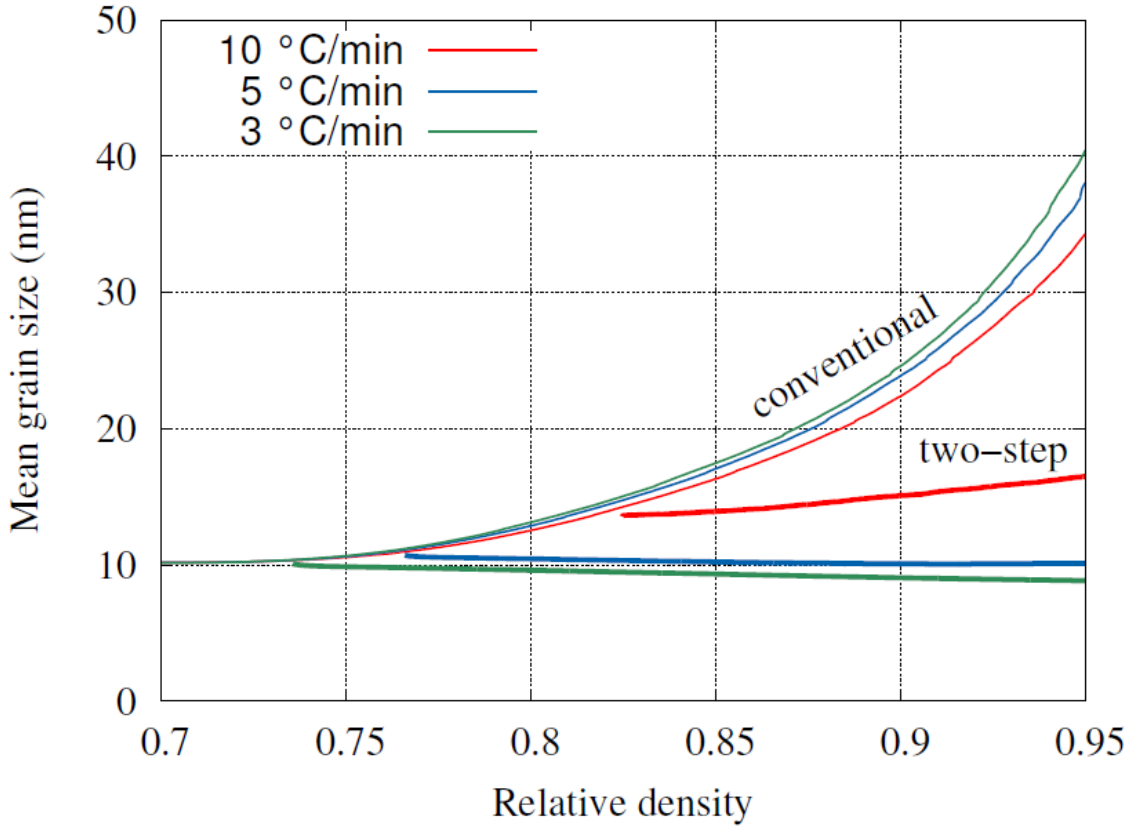

Figure 8: DEM simulation results. Grain size - density trajectories for three heating rates: 3, 5 and 10° C/min obtained by DEM simulations. Two-step sintering curves are represented by thicker lines, while thinner lines represent conventional sintering. The second step is performed at constant temperature after a first heating ramp stage. Sintering temperatures are given in Table 2. A high activation energy for grain boundary mobility ($2.5 \times Q_{GBM}$) is used in the second step as sketched in Fig. 6.

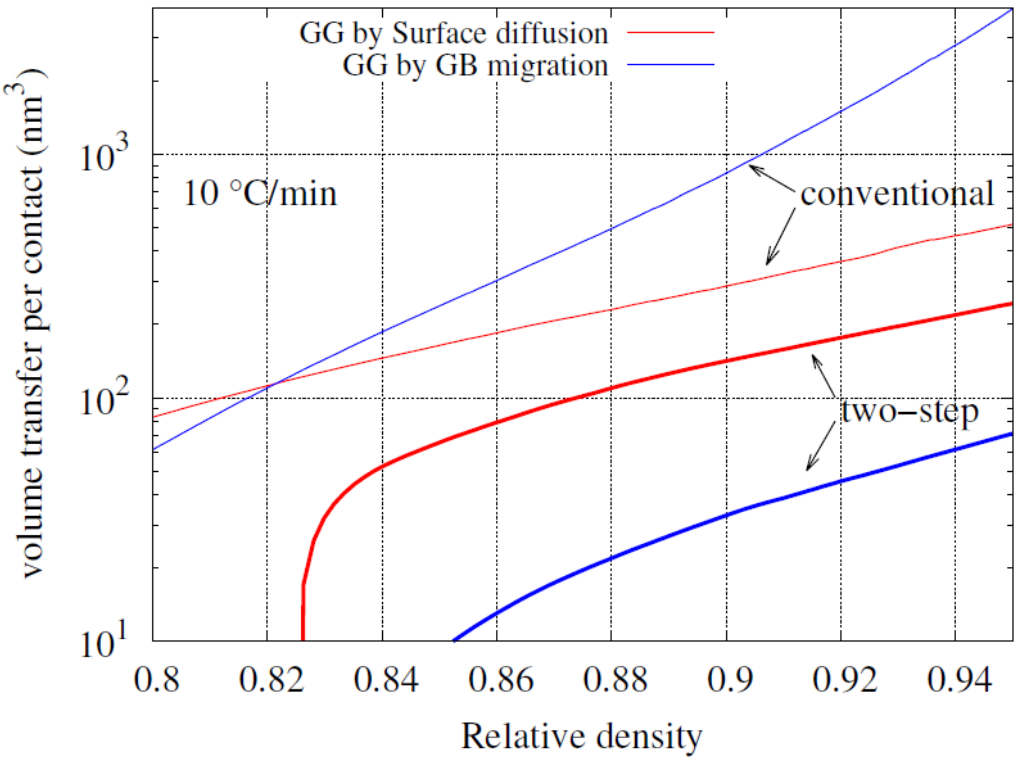

Figure 9: DEM simulation results. Transferred volume per contact for the two grain growth mechanisms considered in the DEM simulations. Comparison between conventional and two-step sintering.

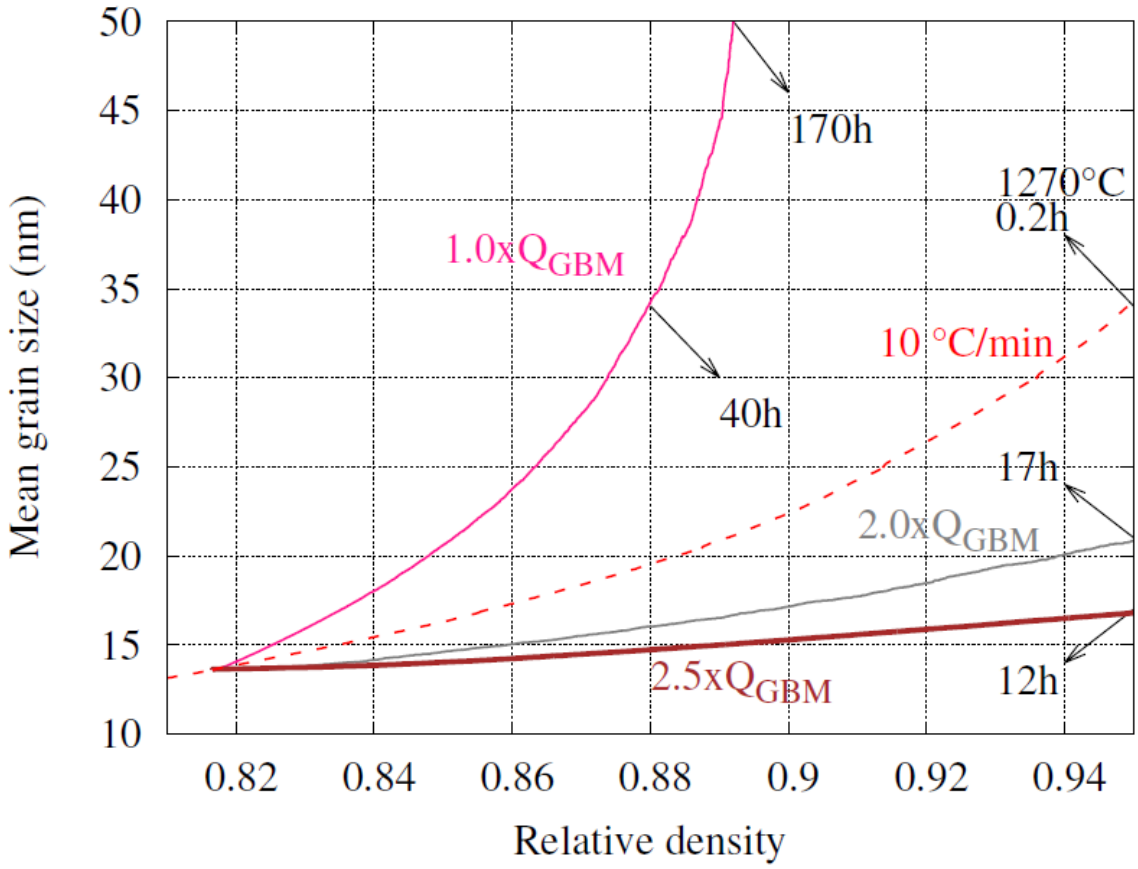

Figure 10: DEM simulation results. Grain size-density trajectories for different Q_{GBM} in the second step at T_2 = 1025° C (solid lines) and in conventional sintering for 10° C/min (dashed line). Times in hour are indicated to illustrate the associated sintering kinetics.

5. Conclusion and outlook

The sintering behaviour, even for only two nanoparticles, can be complex and strongly dependant on the crystalline orientation as shown in [11]. Our discrete model at the particle scale cannot reproduce all the subtleties that can be simulated at the atomic scales. Still, our simulations show good agreement with experimental data in terms of the evolution of the densification rate, density and

grain size. However, the very early densification and grain growth of nano-powders reported by Yang et al. [4] are not correctly reproduced by the model.

A limitation in our discrete modeling is the assumption of spherical particles that indent during sintering. This hypothesis is particularly challenged in the last stage of grain growth where a typical pear shape has been suggested by two-particles modeling [23, 41]. Freeing from this assumption, while keeping the discrete framework, can only be achieved by introducing a new paradigm such as using level-set representation of particles [42].

We observed that for nanoparticles, abnormal grain growth is triggered in our simulations if we enforce the simplistic rule that small particles are always eaten away by larger ones. This phenomenon needs further investigation to clarify the conditions that lead to abnormal grain growth. In particular, molecular dynamics simulations could help (if they are able to model several tens of nanoparticles for large physical times) to detect the conditions that lead to abnormal versus normal grain growth. The transfer of matter from one grain to another is dictated by the local curvature. For spherical grains, as used here, the local curvature is uniquely related to particle sizes. This is clearly simplistic and simulating non-spherical geometries would certainly provide more realistic information about abnormal grain-growth.

With the ability to study thermal cycles during sintering, the model confirms the effectiveness of using fast heating rates to retard grain growth in conventional sintering of nano-powders. The mechanisms underlying the efficiency of two-step sintering of α-alumina and more generally of ceramic oxides still need some further investigation, both from experiments and modelling. Still, this study

plausibly supports the hypothesis of [4] that a transition of the apparent activation energy of the grain boundary mobility is the main reason. Our results suggest that the halting of grain growth in the second step is explained by a large increase (≥ 2.5) of the activation energy of grain boundary mobility for a transition temperature of 1100° C. Further experimental and numerical studies are needed to confirm these values and to clarify whether the cause of the mobility activation energy is the junction drag or some other property of the alumina grain boundary.

Funding: This project has received funding from the European Union's Horizon 2020 research and innovation programme under the Marie Sk lodowskaCurie grant agreement MATHEGRAM No 813202.

Appendix A. Influence of the initial packing particle number

DEM has the ability to handle packings with a large number of particles in a feasible time. Nevertheless, even if millions of particles are considered, this value is much lower than the number of particles used in experiments. It is thus necessary to choose a number of particles that lead to a representative behavior of the real experimental packing. The simulation results should converge when increasing the number of particles. This is more critical in simulations of grain growth as the number of particles decreases significantly during sintering. Fig. A.1 shows the evolution of the mean grain size with temperature for packings with initially: 4 000, 40 000 and 400 000 particles. Below 1200° C, all three packings have the same behaviour. As the number of particles continues to

decrease, some discrepancies appear for the two smaller packings. This is critical at the end of sintering for the 4 000 packing, as very few particles remain (only 12 at 1300° C). We note that results converge to the 400 000 packing curve, thus this initial packing is used for all simulations. For a parallel simulation on four CPU cores, the computational time is approximately five days.

Appendix B. Calculation of the mean grain size

The simplest method to compute the mean grain size in our DEM simulations is to perform the average of the diameter over all particles, which are considered as perfect spheres (with the indented volume kept in the calculation to account for material deposition at the neck). In experiments, starting from microstructural observations, significantly different approaches are used to deal with real non-spherical shapes. To illustrate this, the DEM packings (indented spheres inverted with torus necks shape [43]) are rendered in 3D and exported in the form of RAW image stacks (see Fig. 7). To estimate the mean grain size, we use the granulometric analysis method [44], a widely used approach in image processing to estimate the size of structural features.

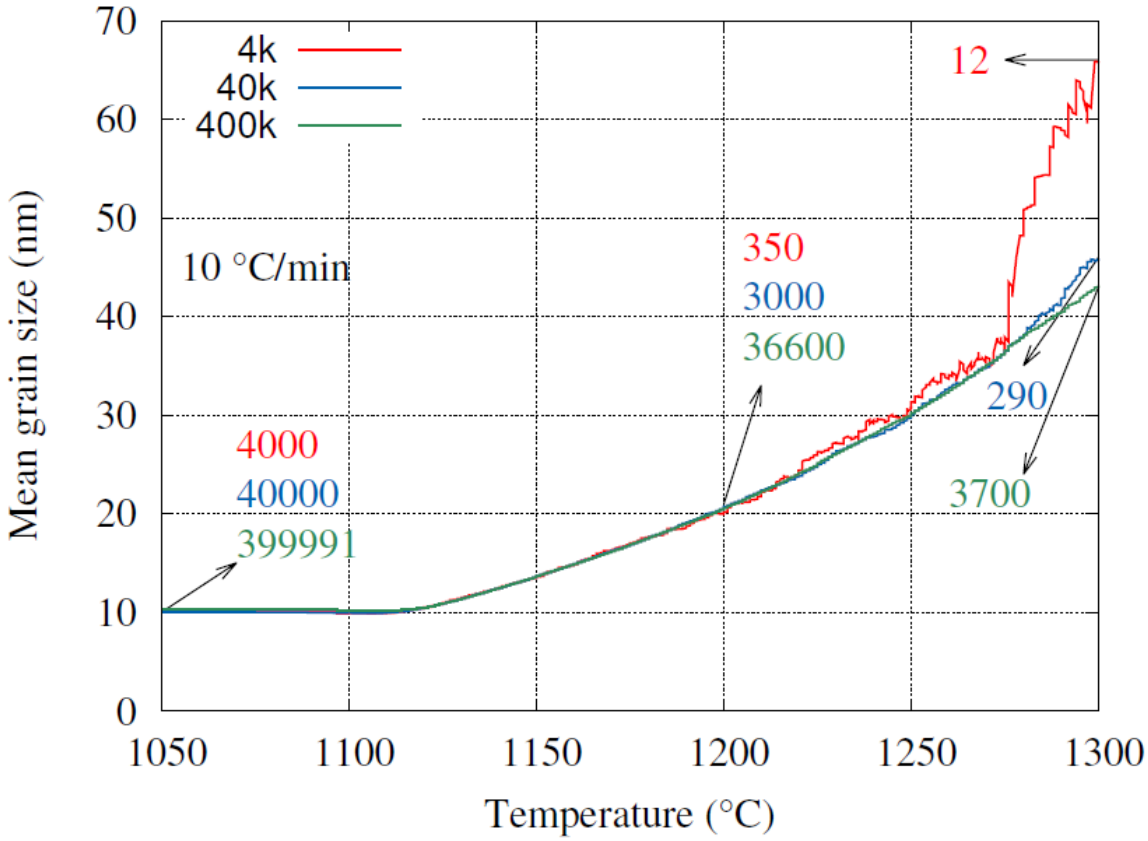

Figure A.1: Evolution of the mean grain size with temperature for increasing number of particles in the initial packing (4 000, 40 000 and 400 000). The number of particles remaining for each packing is indicated at 1050, 1200 and 1300° C.

This image analysis is computationally feasible if the number of particles in the images is around a few thousands. For this purpose, we use packings with initially 4 000 and 40 000 particles for the initial and intermediate stage of sintering respectively. In Appendix A, we have shown that the results are similar to the 400 000 packing at those stages. The granulometry algorithm in the GrainFind module of GeoDict [45] is then capable of evaluating the size of grains, first by converting the image stacks into a distance map by Euclidean distance transform (EDT) and then by fitting pre-defined spheres into the structure. The

spheres are successively fitted into the grain volume in a descending order, thus giving an estimation of their diameters. In that sense, it is a purely geometrical measurement as it does not require knowledge of the characteristics of individual grains and non-spherical complex grains can be assigned the diameters of the largest spheres that can be inscribed.

References

[1] S.-J. L. Kang, Sintering Densification, Grain Growth, and Microstructure, Butterworth-Heinemann, Oxford, 2005. doi:https://doi.org/10.1016/B978-075066385-4/50000-5.

[2] R. K. Bordia, S. J. L. Kang, E. A. Olevsky, Current understanding and future research directions at the onset of the next century of sintering science and technology, Journal of the American Ceramic Society 100 (6) (2017) 2314–2352. doi:10.1111/jace.14919.

[3] G. Bernard-Granger, C. Guizard, New relationships between relative density and grain size during solid-state sintering of ceramic powders, Acta Materialia 56 (20) (2008) 6273–6282. doi:10.1016/j.actamat.2008.08.054.

[4] H. Yang, L. Li, Y. Li, B. Shen, Y. Kang, L. Zhao, J. Li, Y. Dong, J. Li, Unveiling exceptional sinterability of ultrafine α- Al2O3 nanopowders, Journal of Materiomics 7 (4) (2021) 837–844. doi:10.1016/j.jmat.2020.12.011.

[5] N. J. Lo´h, L. Sim˜ao, C. A. Faller, A. De Noni, O. R. Montedo, A review of two-step sintering for ceramics, Ceramics International 42 (11) (2016) 12556–12572. doi:10.1016/j.ceramint.2016.05.065. URL http://dx.doi.org/10.1016/j.ceramint.2016.05.065

[6] X.-H. Wang, I.-W. Chen, Sintering dense nanocrystalline ceramics without final-stage grain growth, Nature 404 (9 March) (2000) 168–171. URL https://www.nature.com/articles/35004548

[7] Y. Dong, H. Yang, L. Zhang, X. Li, D. Ding, X. Wang, J. Li, J. Li, I. W. Chen, Ultra-Uniform Nanocrystalline Materials via Two- Step Sintering, Advanced Functional Materials 31 (1) (2021) 1–9. doi:10.1002/adfm.202007750.

[8] G. Gottstein, V. Sursaeva, L. S. Shvindlerman, Effect of triple junctions on grain boundary motion and grain microstructure evolution, Interface Science 7 (3) (1999) 273–283. doi:10.1023/a:1008721426104.

[9] S. G. Protasova, G. Gottstein, D. A. Molodov, V. G. Sursaeva, S. Shvindlerman, Triple junction motion in aluminum tricrystals, Acta Materialia 49 (2001) 2519–2525.

[10] Y. Dong, I. W. Chen, Mobility transition at grain boundaries in two- step sintered 8 mol yttria-stabilized zirconia, Journal of the American Ceramic Society 101 (5) (2018) 1857–1869. doi:10.1111/jace.15362.

[11] L. Ding, R. L. Davidchack, J. Pan, A molecular dynamics study of sintering between nanoparticles, Computational Materials Science 45 (2) (2009) 247–256. doi:10.1016/j.commatsci.2008.09.021. URL http://dx.doi.org/10.1016/j.commatsci.2008.09.021

[12] L. Benabou, X. Wang, Simulation of silver nanoparticles sintering at high temperatures based on theoretical evaluations of surface and grain boundary mobilities, International Journal for Computational Methods in Engineering Science and Mechanics 21 (6) (2020) 331–342. doi:10.1080/15502287.2020.1841334. URL https://doi.org/10.1080/15502287.2020.1841334

[13] F. Raether, G. Seifert, H. Ziebold, Simulation of Sintering across Scales, Adv. Theory Simulations 2 (7) (2019) 1–19. doi:10.1002/adts.201900048.

[14] B. Paredes-Goyes, D. Jauffres, J.-M. Missiaen, C. L. Martin, Grain growth in sintering: a discrete element model on large packings, Acta Materialia 218 (2021) 117182. doi:10.1016/j.actamat.2021.117182. URL https://doi.org/10.1016/j.actamat.2021.117182

[15] C. L. Martin, L. C. R. Schneider, L. Olmos, D. Bouvard, Discrete element modeling of metallic powder sintering, Scripta Mater. 55 (2006) 425–428.

[16] B. Henrich, A. Wonisch, T. Kraft, M. Moseler, H. Riedel, Simulations of the influence of rearrangement during sintering, Acta Materialia 55 (2) (2007) 753–762. doi:10.1016/j.actamat.2006.09.005.

[17] C. Wang, S. H. Chen, The influence of agglomerates on the densification and microstructural evolution in sintering of a multi-particle system, Science China: Physics, Mechanics and Astronomy 55 (6) (2012) 1051– 1058. doi:10.1007/s11433-012-4743-4.

[18] S. Nosewicz, J. Rojek, K. Pietrzak, M. Chmielewski, Viscoelastic discrete element model of powder sintering, Powder Technology 246 (2013) 157–168. doi:10.1016/j.powtec.2013.05.020. URL http://dx.doi.org/10.1016/j.powtec.2013.05.020

[19] R. Besler, M. Rossetti Da Silva, J. J. Do Rosario, M. Dosta, S. Heinrich, R. Janssen, Sintering Simulation of Periodic Macro Porous Alumina, Journal of the American Ceramic Society 98 (11) (2015) 3496–3502. doi:10.1111/jace.13684.

[20] H. Xin, W. C. Sun, J. Fish, Discrete element simulations of powder-bed sintering-based additive manufacturing, International Journal of Mechanical Sciences 149 (November 2017) (2018) 373–392. doi:10.1016/j.ijmecsci.2017.11.028. URL https://doi.org/10.1016/j.ijmecsci.2017.11.028

[21] T. Matsuda, Development of a DEM taking account of neck increments caused by surface diffusion for sintering and application to analysis of the initial stage of sintering, Computational Materials Science 196 (February) (2021)

110525. doi:10.1016/j.commatsci.2021.110525. URL https://doi.org/10.1016/j.commatsci.2021.110525

[22] D. Bouvard, R. M. McMeeking, Deformation of Interparticle Necks by Diffusion-Controlled Creep (1996). doi:10.1111/j.11512916.1996.tb07927.x.

[23] J. Pan, H. Le, S. Kucherenko, J. A. Yeomans, A model for the sintering of spherical particles of different sizes by solid state diffusion, Acta Materialia 46 (13) (1998) 4671–4690. doi:10.1016/S1359-6454(98)00144-X.

[24] H. Ch'ng, J. Pan, Sintering of particles of different sizes, Acta Materialia 55 (3) (2007) 813–824. doi:10.1016/j.actamat.2006.07.015. URL http://linkinghub.elsevier.com/retrieve/pii/S1359645406005337

[25] A. Bhattacharya, Y. F. Shen, C. M. Hefferan, S. F. Li, J. Lind, R. M. Suter, C. E. Krill, G. S. Rohrer, Grain boundary velocity and curvature are not correlated in Ni polycrystals, Science 374 (6564) (2021) 189–193. doi:10.1126/science.abj3210.

[26] B. V. Derjaguin, V. M. Muller, Y. P. Toporov, Effect of contact deformations on adhesion of particles, J. Colloid Interface Sci. 53 (1975) 314–326.

[27] C. L. Martin, R. K. Bordia, Influence of adhesion and friction on the geometry of packings of spherical particles, Phys. Rev. E 77 (2008) 31307.

[28] D. Bouvard, R. M. McMeeking, The deformation of interparticle necks by diffusion controlled creep, J. Am. Ceram. Soc. 79 (1996) 666–672.

[29] O. A. Ruano, J. Wadsworth, O. D. Sherby, Deformation of fine-grained alumina by grain boundary sliding accommodated by slip, Acta Materialia 51 (12) (2003) 3617–3634. doi:10.1016/S1359-6454(03)00180-0.

[30] W. M. Robertson, R. Chang, The kinetics of grain-boundary groove growth on alumina surfaces, in: W. W. Kriegel, H. Palmour (Eds.), The Role of Grain Boundaries and Surfaces in Ceramics, Springer US, Boston, MA, 1966, pp. 49–60.

[31] S. J. Dillon, M. P. Harmer, Intrinsic grain boundary mobility in alumina, Journal of the American Ceramic Society 89 (12) (2006) 3885–3887. doi:10.1111/j.1551-2916.2006.01331.x.

[32] A. Tsoga, P. Nikolopoulos, Groove Angles and Surface Mass Transport in Polycrystalline Alumina, Journal of the American Ceramic Society 77 (4) (1994) 954–960. doi:10.1111/j.1151-2916.1994.tb07252.x.

[33] J. D. Hansen, R. P. Rusin, M. Teng, D. L. Johnson, Combined-Stage Sintering Model, Journal of the American Ceramic Society 75 (5) (1992) 1129–1135. doi:10.1111/j.1151-2916.1992.tb05549.x.

[34] X. Li, L. Zhang, Y. Dong, R. Gao, M. Qin, X. Qu, J. Li, Pressureless two- step sintering of ultrafine-grained tungsten, Acta Materialia 186 (2020) 116–123. doi:10.1016/j.actamat.2020.01.001.

[35] K. A. Berry, M. P. Harmer, Effect of MgO Solute on Microstructure Development in Al2O3, Journal of the American Ceramic Society 69 (2) (1986) 143–149. doi:10.1111/j.1151-2916.1986.tb04719.x.

[36] S. I. Bae, S. Baik, Sintering and grain growth of ultrapure alumina, Journal of Materials Science 28 (15) (1993) 4197–4204. doi:10.1007/BF00351254.

[37] S. J. Bennison, M. P. Harmer, Effect of Magnesia Solute on Surface Diffusion in Sapphire and the Role-of Magnesia in the Sintering of Alumina, Journal of the American Ceramic Society 73 (4) (1990) 833–837. doi:10.1111/j.1151-2916.1990.tb05122.x.

[38] J. Ro¨del, A. M. Glaeser, Anisotropy of Grain Growth in Alumina, Journal of the American Ceramic Society 73 (11) (1990) 3292–3301. doi:10.1111/j.1151-2916.1990.tb06452.x.

[39] J. Zhao, M. P. Harmer, Effect of Pore Distribution on Microstructure Development: III, Model Experiments, Journal of the American Ceramic Society 75 (4) (1992) 830–843. doi:10.1111/j.1151-2916.1992.tb04148.x.

[40] Z. Z. Fang, H. Wang, V. Kumar, Coarsening, densification, and grain growth during sintering of nano-sized powders—A perspective, International Journal of Refractory Metals and Hard Materials 62 (2017) 110–117. doi:10.1016/j.ijrmhm.2016.09.004. URL http://dx.doi.org/10.1016/j.ijrmhm.2016.09.004

[41] V. Kumar, Z. Z. Fang, P. C. Fife, Phase field simulations of grain growth during sintering of two unequal-sized particles, Materials Science and Engineering A 528 (1) (2010) 254–259. doi:10.1016/j.msea.2010.08.061.

[42] R. Kawamoto, E. Ando`, G. Viggiani, J. E. Andrade, Level set discrete element method for three-dimensional computations with triaxial case study, Journal of the Mechanics and Physics of Solids 91 (2016) 1–13. doi:10.1016/j.jmps.2016.02.021. URL http://dx.doi.org/10.1016/j.jmps.2016.02.021

[43] Z. Yan, C. L. Martin, O. Guillon, D. Bouvard, C. S. Lee, Microstructure evolution during the co-sintering of Ni/BaTiO3 multilayer ceramic capacitors modeled by discrete element simulations, Journal of the European Ceramic Society 34 (13) (2014) 3167–3179. doi:10.1016/j.jeurceramsoc.2014.04.013.

[44] J. Chermant, M. Coster, Granulometry and Granulomorphy by Image Analysis, Acta Stereologica 10 (1991) 7–23. URL http://popups.ulg.ac.be/0351-580X/index.php?id=2049

[45] Becker, J., Biebl, F., Glatt, E., Cheng, L., Grießer, A., Groß, M., Linden, S., Mosbach, D., Wagner, C., Weber, A., Westerteiger, R., Geodict Image processing platform, GeoDict (Release 2022) [Simulation software] Math2Market GmbH, doi.org/10.30423/release.geodict2022 (2021).